

www.acsanm.org Article

Unraveling the Role of Grain Boundary Anisotropy in Sintering: Implications for Nanoscale Manufacturing

Omar Hussein, Maher Alghalayini, Shen J. Dillon, and Fadi Abdeljawad*



Cite This: ACS Appl. Nano Mater. 2021, 4, 8039–8049



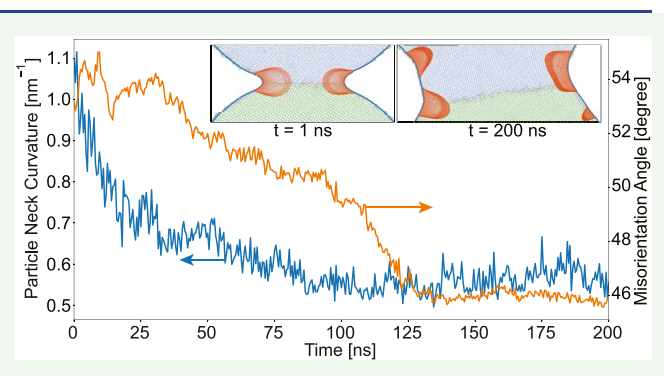
ACCESS

Metrics & More

Article Recommendations

Supporting Information

ABSTRACT: Sintering is a thermal processing technique used to consolidate particle compacts into structures broadly used in optical, catalytic, electronic, and structural applications. Of particular interest is the sintering of nanocrystalline particles, as it leads to reduced sintering temperatures and faster processing times and it enables the fabrication of bulk nanostructured or nanoporous materials. However, the lack of knowledge of the role of grain boundary (GB) geometry in sintering rates limits our ability to manipulate densification and coarsening processes. Herein, we leverage atomistic simulations to investigate the sintering behavior of a series of [001] tilt GBs in Ni over 200 ns using the two-particle geometry. The energy and self-diffusion for



these GBs are calculated, and several geometric features describing the morphological evolution are tracked over time. Particle rotation, resulting in the temporal evolution of GB misorientation, is observed in several systems. Our results show large variations in particle neck growth and shrinkage rates as a function of GB type and suggest faster sintering rates with increased GB misorientation angle. Further, it is found that nanoparticles sinter at a much slower rate than predicted from GB-based sintering models, suggesting that the process is not dominated by a single mechanism. As a measure of sintering stress, we track the temporal evolution of particle neck curvatures, which are shown to decrease over time at a rate dependent on GB geometry. In broad terms, our simulation results provide future avenues to employ particle orientations and resultant GB types as a strategy to fabricate sintered materials with controlled nanostructured features.

KEYWORDS: nanoscale sintering, grain boundary, nanoparticles, atomistic simulations, particle rotation, anisotropy

INTRODUCTION

Sintering is a thermal processing technique used to consolidate powder compacts and convert them into systems with enhanced strength and structural integrity. The main thermodynamic driving force for pressure-less solid-state sintering is the reduction in the interfacial contribution to the total free energy of the sintered body. 1,2 In recent years, sintering of nanoscale particles has received considerable attention as it presents many potential advantages, such as lower processing temperatures³ and shorter sintering times.⁴ Further, several emerging additive manufacturing techniques, such as direct ink write⁵ and aerosol jet printing,⁶ which employ sintering as a processing step, have demonstrated the ability to manufacture bulk and lattice nanostructured objects. The integration of nanostructures with such manufacturing technologies offers unique advances in the design of novel materials combining crystal size-dependent properties and design freedom, thereby enabling a myriad of applications, including miniaturized electronics,8 battery electrodes,9 and catalysis.

In nanocrystalline particle compacts, the role of material interfaces is amplified owing to the increased surface-to-

volume ratio and the number of contact points between particles. In general, two interface-driven processes accompany solid-state sintering, namely densification (i.e., elimination of internal porosity) and coarsening (i.e., free surface smoothing and grain growth), and the ability to manipulate these during sintering is considered a key aspect of microstructure control. For example, it is desirable to suppress densification in technologies requiring high surface area, such as catalysts and electrode materials, while full densification is a key processing requirement in structural applications.

Analytical models of idealized geometries provide the basis for the current understanding of sintering by relating the temporal evolution of a microstructural feature of interest to process parameters, materials properties, and transport mechanisms. The treatments by Herring² and Nichols and

Received: May 19, 2021 Accepted: June 25, 2021 Published: July 19, 2021





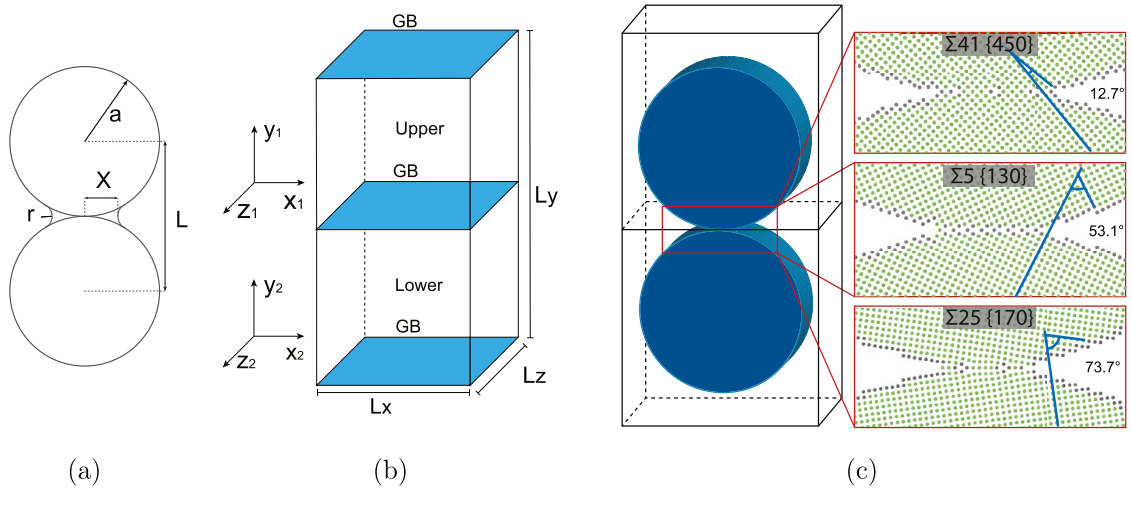


Figure 1. Schematic depicting the (a) geometric parameters in the two-particle sintering system, (b) atomistic bicrystal system used in GB energy and self-diffusion calculations, and (c) atomistic two-particle geometry that is carved out from the system in (b). The insets in (c) show close-up views at some of the GB systems explored in this work.

Mullins¹² examined the role of surface energy and curved surfaces in sintering. In crystalline particles, the formation and growth of grain boundaries (GBs) at particle neck regions during sintering introduces several effects that markedly alter the configuration of a particle compact and its internal porosity. 13 First, the GB energy contributes to the energetics of the sintered body and, as a result, affects the driving force for sintering processes.¹⁴ Second, GBs act as point defect sources and sinks, which in turn influence mass transport and fluxes.¹⁵ Finally, GBs serve as short-circuit diffusion pathways with an activation energy that is distinct from the bulk. Wakai et al. 16 developed an experimental technique to investigate the role of GB diffusion and energy in the sintering behavior. Experimental studies demonstrated GB-driven particle rearrangement during sintering.¹⁷ High-resolution microscopy techniques were recently used to measure single GB diffusivity and point defect formation volume and reveal the discrete nature of sintering, which is indicative of GB defect-mediated mechanisms. 18,19

Several particle configurations, such as the two- $^{20-22}$ and three-particle 23 geometries and particle on a substrate, 24 have been used to examine the microstructural evolution during sintering. With the two-particle geometry (refer to Figure 1a), geometric features, such as the particle neck width X and radius r, and distance between particles' centers of mass L describe the morphological evolution and provide a measure of densification and coarsening that accompany sintering. With this geometry, the chemical potential at the particle-free surface $\mu_{\rm S}$ and that at the particle neck region, where a GB meets the free surface, $\mu_{\rm N}$ are given by 25,26

$$\mu_{\rm S} = -\Omega \gamma_{\rm s} \left(\frac{2}{a}\right) \tag{1a}$$

$$\mu_{\rm N} = -\Omega \sigma = -\Omega \gamma_{\rm s} \left(\frac{1}{r} - \frac{\sqrt{\left(1 - (\gamma_{\rm gb}/2\gamma_{\rm s})^2\right)}}{X} \right) \tag{1b}$$

where σ is the sintering stress, 25,27 γ_s and $\gamma_{\rm gb}$ denote the free surface and GB energy, respectively, a is the particle radius, and Ω is the atomic volume. Variations in the sintering stress between regions at free surfaces, $2\gamma_s/a$, and the one at particle

neck regions, σ , introduce gradients in the chemical potential, which in turn lead to mass fluxes along particle surfaces. For the two-particle spherical geometry and assuming a single dominant mass transport mechanism, dynamical scaling relations were derived for the particle neck width X and linear shrinkage $\Delta L/L_o = (L_o - L)/L_o$ and are written as 1,25

$$\left(\frac{X}{a}\right)^m = \frac{H}{a^n}t\tag{2a}$$

$$\left(\frac{\Delta L}{L_o}\right)^{m/2} = \frac{H}{2^m a^n} t \tag{2b}$$

where $L_{\rm o}$ is the initial distance between the particles' centers and H is a parameter encompassing several materials properties. (m, n) are the scaling law exponents that depend on the assumed mass transport mechanism. $^{20-22}$ It is worth noting that in such analytical models, the axisymmetry assumption is invoked, where mass transport is assumed independent of the polar, or rotation, angle within the GB plane and only depends on the radial distance from the GB center $^{2.5}$ (see Figure S1 in the Supporting Information).

Theoretical and computational studies 14,28–33 investigated the microstructural evolution during sintering. For example, a study by Djohari and Derby demonstrated the complex mass transport mechanisms that accompany sintering. Using the three-particle geometry, it was found that the relative GB to free surface energy plays an important role in particle neck growth and densification rates. While the aforementioned studies provide insights into several factors influencing sintering kinetics, they do not account for the role of GB structure and anisotropic GB properties in sintering rates.

In recent years, atomistic simulations of several materials systems, including Cu,³⁴ Au,³⁵ Ag,³⁶ Al,^{36,37} Ni,³⁸ Fe,³⁹ and W,⁴⁰ have been used to gain fundamental insights into the early stages of particle neck formation with a primary focus on the role of temperature,^{34,40} particle size,^{41,42} and sintering-induced phase transformations.⁴³ For example, accelerated sintering rates in Cu nanoparticles were observed with increasing temperature.³⁴ The abovementioned atomistic studies, however, do not quantify the role of GB character in sintering kinetics. In general, five macroscopic degrees of

Table 1. For the Atomistic Bicrystal Geometry, the \sum value, Crystal x-Axis for the Upper x_1 and Lower x_2 Crystals, Misorientation Angle θ , 0 K GB Energy, and GB Self-Diffusion $D_{\rm gb}$ at 1000 K^a

[001] tilt GBs				
∑ value	$\mathbf{x}_1/\mathbf{x}_2 \ [hkl]_{\mathrm{upper}}/[hkl]_{\mathrm{lower}}$	θ (deg)	energy (10^{-3} J/m^2)	$D_{\rm gb}$ at 1000 K (10 ⁻¹⁰ m ² /s)
41	[540]/[450]	12.68	839.74	0.3733
25	$[4\overline{3}0]/[3\overline{4}0]$	16.26	946.69	0.4684
149	$[10\overline{7}0]/[71\overline{0}0]$	20.02	1050.78	0.7519
13	$[3\overline{2}0]/[2\overline{3}0]$	22.62	1091.26	0.9973
17	$[5\overline{3}0]/[3\overline{5}0]$	28.07	1180.12	2.4547
53	$[5\overline{9}0]/[9\overline{5}0]$	31.89	1255.48	6.2742
5	$[\overline{31}0]/[\overline{3}10]$	36.87	1218.12	4.0483
29	$[5\overline{2}0]/[2\overline{5}0]$	46.40	1336.15	12.7478
5	$[\overline{21}0]/[\overline{2}10]$	53.13	1284.61	9.1195
17	$[4\overline{1}0]/[1\overline{4}0]$	61.93	1240.94	6.3347
13	$[5\overline{1}0]/[1\overline{5}0]$	67.38	1200.55	4.5865
25	$[7\overline{1}0]/[1\overline{7}0]$	73.74	1102.26	3.2630
41	$[9\overline{1}0]/[1\overline{9}0]$	77.32	1007.16	3.8964
61	$[560]/[\overline{5}60]$	79.61	741.58	0.3293

^aThe crystal z-axis is [001] for both particles in all systems.

freedom (DOF) characterize the geometry of a GB; three describe the GB misorientation and two define the GB plane normal. How Numerous studies have shown a strong dependence of several GB properties, such as energy, on the boundary's DOF. Therefore, quantifying the role of GBs in the morphological evolution and sintering processes is a critical piece to advancing our understanding of nanoscale sintering. Indeed, a recent review by Bordia et al. suggested the need to extend existing sintering treatments to account for the role of interfaces and their structures in sintering processes.

In this work, we leverage molecular dynamics (MD) simulations to investigate the role of GB character in the sintering of nanoscale particles. More specifically, we examine the behavior of [001] tilt GBs in Ni in the sintering of the two-particle geometry. The sintering behavior of a system with a $\sum 3$ {111} coherent twin GB is also explored, as this GB exhibits one of the lowest GB energies. The temporal evolution of several geometric features is obtained to quantify coarsening and densification processes as a function of GB character.

■ COMPUTATIONAL METHODS

In this work, molecular dynamics (MD) simulations are performed using the Ni embedded atom method (EAM) interatomic potential developed by Foiles and Hoyt, 46 which yields bulk thermodynamic (e.g., lattice constant a = 3.52 Å at 0 K, sublimation energy, bulk modulus, melting point $T_{\rm m}$ = 1565 K) and defect (e.g., vacancy formation energy and stacking fault and surface energies) properties that are in agreement with experimentally determined values.⁴⁶ Further, this interatomic potential was used in prior studies to calculate the energies of several GBs in Ni,45 which showed excellent agreement with experimental values.⁴⁷ Our atomistic simulations employ the GPU implementation of the large-scale atomic/molecular massively parallel simulator $(LAMMPS)^{48}$ and visualizations of the atomic structures are obtained using the Open Visualization Tool (OVITO).⁴⁹ The polyhedral template matching (PTM) algorithm⁵⁰ is used to identify the local structural environment for each atom (e.g., face-centered cube (FCC), hexagonal close packed (HCP)), calculate particle orientations, and reveal GB and free surface atoms. The dislocation extraction algorithm (DXA)⁵¹ is used to identify dislocations in atomistic systems. All molecular dynamics simulations in this work employed a time step of 1 fs.

Generation of GB Structures. A total of 14 [001] symmetric tilt GBs in Ni are employed in this work. In addition, a system with a $\sum 3$

{111} coherent twin GB is constructed, as this GB exhibits one of the lowest GB energies. 45 Ni bicrystal geometries with planar GBs are generated using the γ-surface method. ^{52,53} A fully periodic atomistic system is created from two half-crystals, each of which is rotated about the [001] tilt axis by an equal and opposite angle $\theta/2$, where θ defines the tilt angle. Figure 1b is a schematic illustration of the atomistic bicrystal geometry used in this work. A sequence of relative displacements between the upper and lower half-crystals is used in conjunction with atom deletions and conjugate gradient energy minimizations to identify a low-energy GB configuration. The systems are allowed to expand or contract in the perpendicular direction to the GB plane. For the bicrystals explored in this work, Table S1 in the Supporting Information lists the dimension of the simulation box and number of atoms in each system. To capture the periodicity of each GB atomic structure, the dimension of each bicrystal system is slightly varied to accommodate an integer number of unit cells necessary to model each specific GB. Table 1 lists the \sum value (\sum represents the reciprocal density of coincidence sites within the coincidence site lattice description⁴⁴), the x-axis for the upper (x_1) and lower (x_2) crystals, and GB misorientation angle θ for each of the [001] tilt GBs explored in this work.

Grain Boundary Self-Diffusion. We follow the treatment outlined by Suzuki and Mishin⁵⁴ to calculate GB self-diffusion D_{ob} at 1000 K $(T/T_m = 0.64)$ for all [001] GBs considered in this work. The atomistic bicrystal structures are first uniformly expanded by the thermal expansion of Ni at 1000 K. We then perform a preannealing MD simulation for 1 ns at 1000 K in the NVE ensemble while applying a Langevin thermostat⁵⁵ and Berendsen barostat (using the aniso option in LAMMPS)⁵⁶ to achieve zero pressure on the simulation box (see Figure S2 in the Supporting Information). For diffusion calculations, a thin layer of atoms at the top and bottom edges of the simulation box is fixed to prevent spontaneous GB motion,⁵⁴ and a long MD run (10 ns) is then performed at 1000 K in the NVT ensemble using a Nosé-Hoover thermostat. 57,58 Mean square displacements of atoms $\langle r^2(t) \rangle$ contained in a thin region of $\pm \delta$ ($\delta = 0.5$ nm is used in this work⁵⁴) around the GB core are calculated. Then, Einstein relation is used to calculate the GB selfdiffusion as $D_{\rm gb} = (1/6) \lim_{t \to \infty} d\langle r^2(t) \rangle / dt$.

Sintering of the Two-Particle Geometry. In this study, we employ the two-particle geometry, as it represents an idealized configuration of contact points in real particle compacts, and it has been the geometry of choice in several analytical sintering models.^{20–22} Using 0 K equilibrated bicrystal geometries, we carve out two 20 nm diameter circular disks, referred to thereafter as particles, from these systems, where each particle is carved out from one of the crystals in the bicrystal system. The periodic out-of-plane

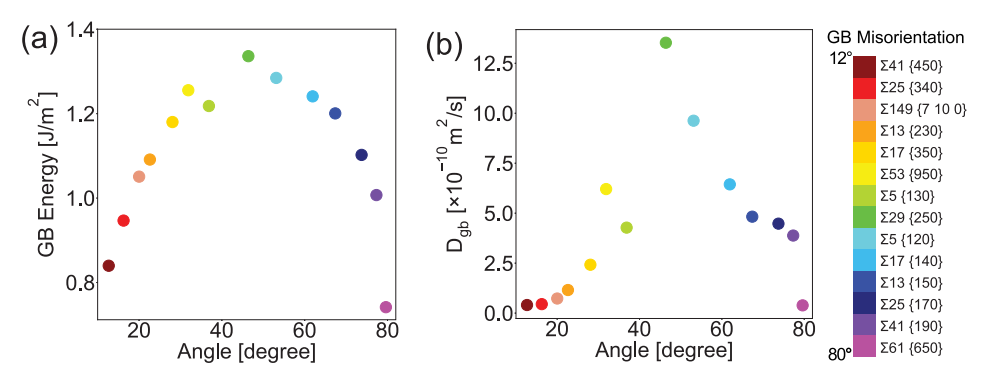


Figure 2. Plot of (a) 0 K GB energy and (b) GB self-diffusion at 1000 K as a function of GB misorientation angle for the [001] tilt GBs explored in this work.

thickness for these systems is chosen to be 22 Å, refer to Figure 1c for a schematic depicting the construction of atomistic two-particle systems. Periodic nanoscale circular disks are used in lieu of threedimensional (3D) particles to circumvent the computational expense associated with simulating 3D particles, each of which would contain millions of atoms. This approach then would enable the simulations of many GB systems to large time scales needed to probe self-similar regimes. Figure S3 in the Supporting Information shows a comparison between the sintering behavior of the circular disk geometry used in this work and that of the 3D spherical particle one for the systems with $\sum 5$ {120} and $\sum 29$ {250} GBs, illustrating similar trends in terms of particle neck growth. Further, Table S2 of the Supporting Information shows scaling analysis comparing computational runtimes of a representative circular disk system and a 3D spherical particle geometry of the same diameter and GB type, where it is shown that the spherical particle geometry requires an order of magnitude more computational resources for each GB system. Finally, it is worth noting that sintering of cylindrical nanorods has been recently demonstrated experimentally.

When constructing two-particle systems, we ensure that both particles meet at the GB with a pre-established particle neck width of ≈2 nm, and this in turn eliminates rapid particle rotations during the temperature ramp-up stage of the sintering process, thereby preserving the misorientation DOF for the GB under consideration. This approach is in contrast with what has been previously done in atomistic studies of sintering, where particles are initially brought into close proximity without pre-established neck regions. ^{34,40} This in turn results in rapid and uncontrolled particle rotations, which render the analysis of the impact of GB character on sintering kinetics difficult.

Then, atomistic two-particle systems are uniformly expanded by the thermal expansion of Ni at 1000 K ($T/T_{\rm m}=0.64$), at which an FCC solid is the stable phase. We then perform isothermal and isobaric integration to march atoms' positions and velocities using a Nosé–Hoover thermostat and barostat at 1000 K and zero pressure along the out-of-plane (cylindrical) direction. This creates a trajectory in phase space that is consistent with the isothermal—isobaric (NPT) ensemble. This isothermal sintering condition is equivalent to immersing a particle compact in a solvent to assist the heat transfer between particles and a heat reservoir. Atomistic sintering simulations are carried out to 200 ns.

Quantitative Microstructural Metrics. To quantify coarsening and densification processes, we examine the temporal evolution of particle neck width (X), linear shrinkage $(\Delta L/L_{\rm o})$, radius of gyration $(R_{\rm g})$, and particle neck curvature (κ) (cf. Figure 1a). In what follows, we highlight each of these metrics.

The particle neck width X is measured using PTM to identify free surface and GB atoms. A small window surrounding the particle neck region is identified and the position of atoms within the particle neck is used to calculate particle neck width. In addition to the structural environment of atoms, PTM is used to obtain the crystallographic orientation of the particles. FCC atoms in each particle are identified, and each particle's center of mass is calculated according to $\overline{\bf r} = \sum_j {\bf r}_j / N_p$, where ${\bf r}_j$ denotes the position vector of the jth atom in the particle

and $N_{\rm p}$ is the number of atoms in the particle. Linear shrinkage $\Delta L/L_{\rm o}$ is obtained from a distance between the two particles' centers with the initial distance $L_{\rm o}=20$ nm, i.e., $\Delta L=L_{\rm o}-L(t)$. The radius of gyration $R_{\rm g}$ is the root mean square distance of atoms from the center of mass of the two-particle system as a whole and is given by $R_{\rm g}^2=\sum_j r_j^2/N_{\rm tot}$, where $r_j=|{\bf r}_j-{\bf r}_{\rm m}|$ and ${\bf r}_{\rm m}$ is the center of mass of the two-particle system and $N_{\rm tot}$ is the total number of atoms in the system. $R_{\rm g}$ describes the spatial distribution of atoms with respect to the center of mass of the two-particle system and is a measure of densification.

According to eq 1a and 1b, the chemical potential and, as a result, mass fluxes are sensitively dependent on the local curvature. To this end, we monitor the temporal evolution of the local particle neck curvatures κ . We start by constructing binary images of the atomistic two-particle systems and then applying a Gaussian filter to smooth free surface profiles and eliminate edges that are associated with atomic steps. Then, we trace boundaries separating regions inside particles from the outside and interpolate a curve along these boundaries. The local curvatures are obtained by fitting polygons along the curves then using analytical expressions for the polygons' curvature. The curvature distributions at particle neck regions are then used to report the average curvature $\langle \kappa \rangle$.

■ RESULTS AND DISCUSSION

We first start by exploring the GB energy and GB self-diffusion coefficients for the [001] tilt boundaries explored in this work. Figure 2a,b shows, respectively, a plot of GB energy and GB self-diffusion $D_{\rm gb}$ as a function of the misorientation angle. Here, we note that GB self-diffusion is calculated at 1000 K. Out of all GBs reported in this work, the $\sum 29$ {250} GB has the largest energy, and it also exhibits the highest GB diffusion coefficient. A general trend is observed, in which high-energy GBs are also ones with high GB self-diffusion coefficients. Similar trends between GB energy and self-diffusion have been previously observed. For example, for [001] tilt GBs in Ag, boundaries with large self-diffusion values 60 are correlated with high-energy GBs. Our GB self-diffusion calculations are consistent with experimentally obtained values in Ni. 62

Then, we qualitatively examine the sintering kinetics of the two-particle geometry with different GB types. Figure 3a–d depicts the temporal evolution of the system with the $\sum 5$ {120} GB at (a) t=0 (initial state), (b) t=1 ns, (c) t=120 ns, and (d) t=200 ns, where atoms colored in red/blue (gray) represent FCC (GB and free surfaces) according to the PTM algorithm. For a better visualization of the structures, atoms in each particle are assigned a unique color (i.e., red or blue). It can be seen that the GB starts to form and grow very rapidly in the initial stages leading to a rapid particle neck growth. At late simulation times, it is observed that particle neck regions, where the GB meets a free surface, develop faceted profiles.

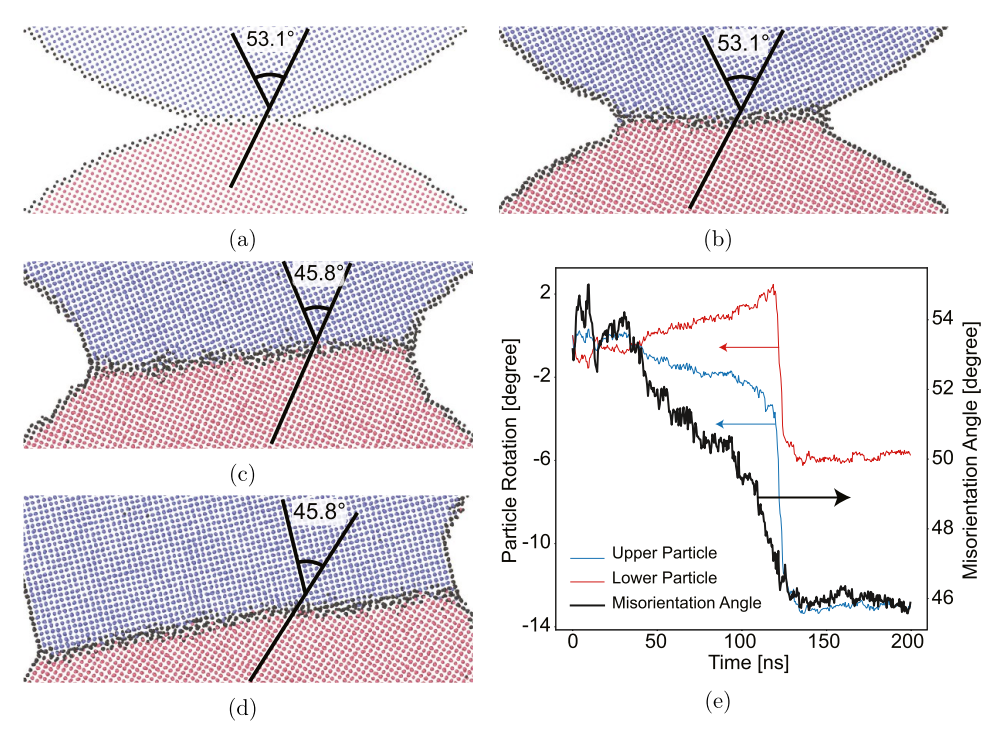


Figure 3. For the two-particle system with a $\sum 5$ {120} GB: (a-d) Close-up views depicting particle neck evolution at (a) t = 0, (b) t = 1 ns, (c) t = 120 ns, and (d) t = 200 ns. Red/blue (gray) represent FCC (GB and free surface) atoms according to the PTM algorithm. Blue (red) corresponds to atoms in the top (bottom) particles. (e) Temporal evolution of both particle rotations and resultant GB misorientation angle.

Further, for this system, the two particles undergo relative rotations during sintering, and at late simulation times, the GB develops an asymmetric profile (cf. Figure 3d) with a measured GB misorientation of $\approx 45.8^{\circ}$ at t = 200 ns. To demonstrate this effect, Figure 3e depicts the temporal evolution of particle rotations and the resultant GB misorientation for the twoparticle system with a $\sum 5$ {120} GB. In the initial stages of GB formation, i.e., from t = 0 to ≈ 50 ns, no considerable crystallographic orientations of the two particles are observed. Then, the two particles start to rotate at different rates leading to changes to the GB misorientation angle. At $t \approx 150$ ns, the GB misorientation reaches a plateau of ≈45.8°. This movie is an animation depicting the evolution of this two-particle system along with particle rotation and particle neck curvature, where the arrows represent normal vectors at points on particle neck regions, and their lengths are scaled by the curvature values at these points. A close examination of Table 1 and Figure 2 shows that the system with this GB evolves to a misorientation angle near the \sum 29 GB misorientation, i.e., θ =

The particle rotation behavior shown in Figure 3 is also observed in other GB systems. For example, Figure 4a–d shows close-up views of particle neck regions at 200 ns for the systems with (a) $\sum 13$ {150}, (b) $\sum 25$ {170}, (c) $\sum 29$ {250}, and (d) $\sum 149$ {7 10 0} GBs, where atoms colored in red/blue (gray) represent FCC (GB and free surfaces) according to the PTM algorithm. The final GB misorientation angle after 200 ns of sintering is also shown in the figure. It can be seen that the particle neck geometry (i.e., width and curvature) varies considerably as a function of GB type. Further, the left and right sides of particle neck regions, where GBs meet free surfaces, develop different geometric profiles. According to eq 1a and 1b, such differences in particle neck geometry result in variations in the local chemical potential, which in turn lead to

differences in mass fluxes between the left and right sides of particle neck regions. To quantify the crystallographic orientations of particles during sintering, Figure 4e shows the initial and final (t = 200 ns) GB misorientation angle for all [001] GBs explored in this work, where blue square (red circle) markers denote initial (final) GB misorientations. It can be seen that systems, such as the ones with $\sum 41 \{190\}$, $\sum 149$ {7 10 0}, and $\sum\!25$ {170} GBs, exhibit little rotation, while others show large changes in GB misorientation during sintering. The largest change in GB misorientation is observed to be $\approx 10^{\circ}$, such as in two-particle systems with $\sum 17 \{350\}$ and $\sum 13$ {320} boundaries. The results depicted in Figures 3 and 4 suggest that sintering of nanoscale particles could result in particle rotations away from symmetric and low-energy GB structures. This effect is driven by the large sintering driving forces in nanoscale particles and is expected to be less dominant in micron-sized particles.³⁵ Particle rotations during sintering have been experimentally observed in particle compacts¹⁷ and particle on a substrate geometry.⁶³ Moreover, for particles less than 10 nm in size, mechanisms, such as surface melting 40,42 and deformation twinning, 64 have been found to influence particle rotation.

Another example deals with the two-particle system with a $\sum 3$ {111} GB, in which the particle neck region is found to grow through nucleation of GB defects, leading to discrete jumps in particle neck width. Figure 4f—g shows close-up views depicting the particle neck region for this system in the initial stage t=0 (Figure 4f) and at a simulation time t=1 ns (Figure 4g). The PTM algorithm is used to identify the local structural environment for each atom, where green (gray) denotes FCC (no ordering) and the row of atoms in red represent this coherent twin GB. In the very early stages of sintering, partial dislocations with an edge character according to DXA nucleate from the GB into the bulk leaving behind faulted planes (HCP

ACS Applied Nano Materials

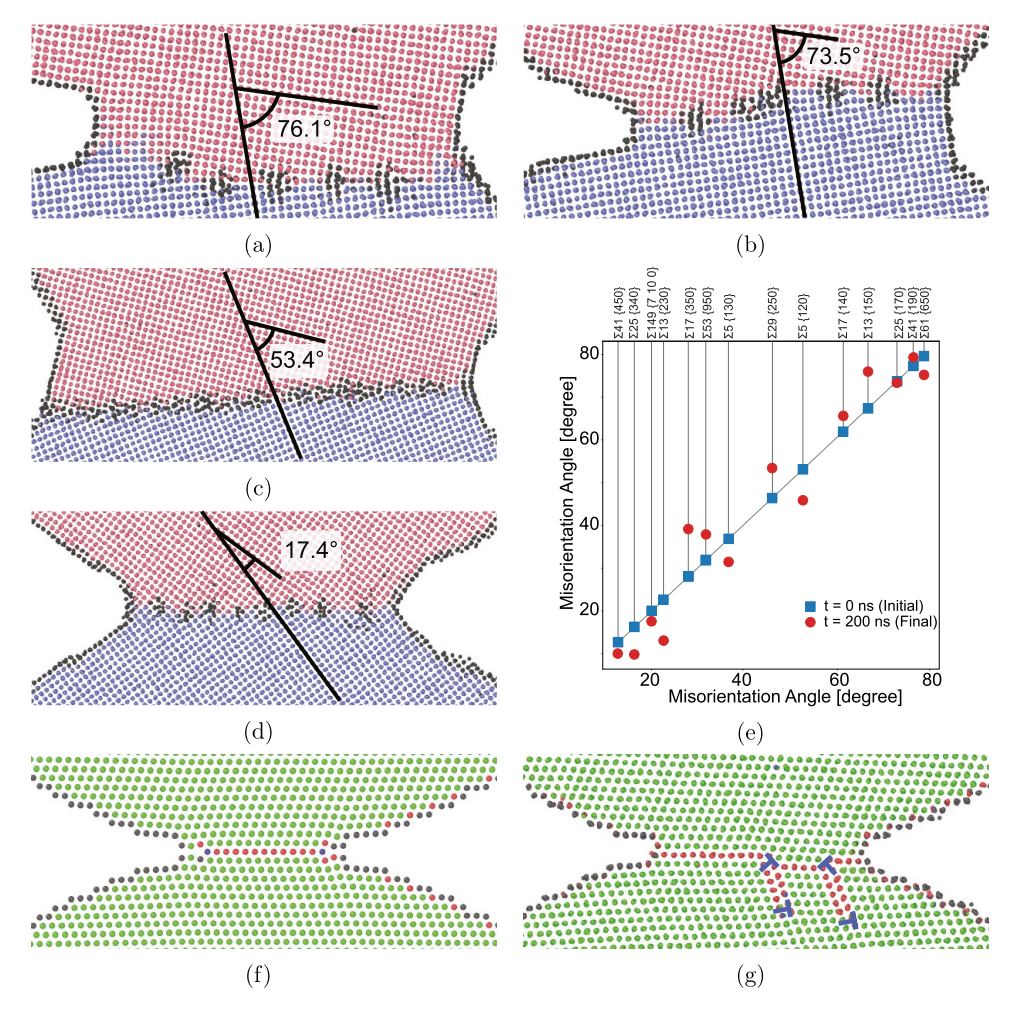


Figure 4. (a–d) At a sintering time of 200 ns, close-up views depicting particle neck regions for two-particle systems with (a) $\sum 13$ {150}, (b) $\sum 25$ {170}, (c) $\sum 29$ {250}, and (d) $\sum 149$ {7 10 0} GB. Red/blue (gray) represent FCC (GB and free surface) atoms according to PTM. Red (blue) corresponds to atoms in the top (bottom) particles. (e) For all [001] GBs explored in this work, a plot of the GB misorientation angle in the initial stage (blue squares) and final one (red circles) at a simulation time of 200 ns. (f–g) For the two-particle system with a $\sum 3$ {111} GB, close-up views depicting particle neck regions at (f) t = 0 and (g) t = 1 ns. Atoms are colored according to PTM, where green (gray) denotes FCC (GB/free surface) and red denotes HCP at the coherent twin GB. During sintering, dislocations in blue nucleate at the GB and extend in the bulk leaving behind stacking faults.

ordering), which are colored in red in Figure 4g. Four dislocation lines are identified in Figure 4g; two are at the GB creating a boundary step and two in the bulk, where the stacking faults terminate. As will be shown in Figure 5, the nucleation of these dislocations at an early sintering time leads to a "burst" in particle neck growth and linear shrinkage. For this GB system, no further linear shrinkage $\Delta L/L_{\rm o}$ is observed, at least for the simulation times attained in this work. This suggests that sintering for this GB system is interface reaction rate-limited.

We now direct our attention to the temporal evolution of particle neck width X, linear shrinkage $\Delta L/L_{\rm o}$, and gyration radius $R_{\rm g}$, where the results are depicted in Figure 5. Figure 5a is a plot of the temporal evolution of particle neck width X, where large variations in X profiles can be seen as a function of GB character. It is observed that the two-particle system with the $\sum 5$ {120} GB shows the fastest particle neck growth, followed by the systems with $\sum 29$ {250}, $\sum 53$ {950}, and $\sum 5$ {130} GBs. According to Figure 2, these GBs are characterized by the largest GB self-diffusion coefficients out of all GBs explored in this work. For the system with a $\sum 5$ {120} GB, the large increase in X at ≈ 120 ns corresponds to a large change in

particles' orientations and the resultant change in both GB misorientation (cf. Figure 3e) and structure from a symmetric boundary to an asymmetric one. On the other hand, the system with a $\sum 3$ {111} GB exhibits sluggish particle neck growth kinetics, where a small increase in X is observed in the initial sintering stage due to defect nucleation events from the GB, then the particle neck profile shows a near flat behavior. Also, an example of the temperature dependence of particle neck growth is shown in Figure S4 in the Supporting Information for the system with a $\sum 29$ {250} GB, where enhanced neck growth is observed with increased temperature, an effect that has been observed in prior atomistic studies of two-particle sintering. ^{34,40}

The next geometric feature we explore is the gyration radius $R_{\rm g}(t)$, which quantifies the evolution of the atoms with respect to the center of mass of the two-particle system, and can be used as a measure of densification. Figure 5b is a plot of $R_{\rm g}(t)$ for all systems explored in this work. It can be seen that $R_{\rm g}(t)$ decreases with respect to its initial value $R_{\rm g}(0)$ indicating that atoms in each two-particle system evolve to become more clustered around the two-particle system's center of mass. Similar to particle neck growth trends, systems with $\sum 5$ {120},

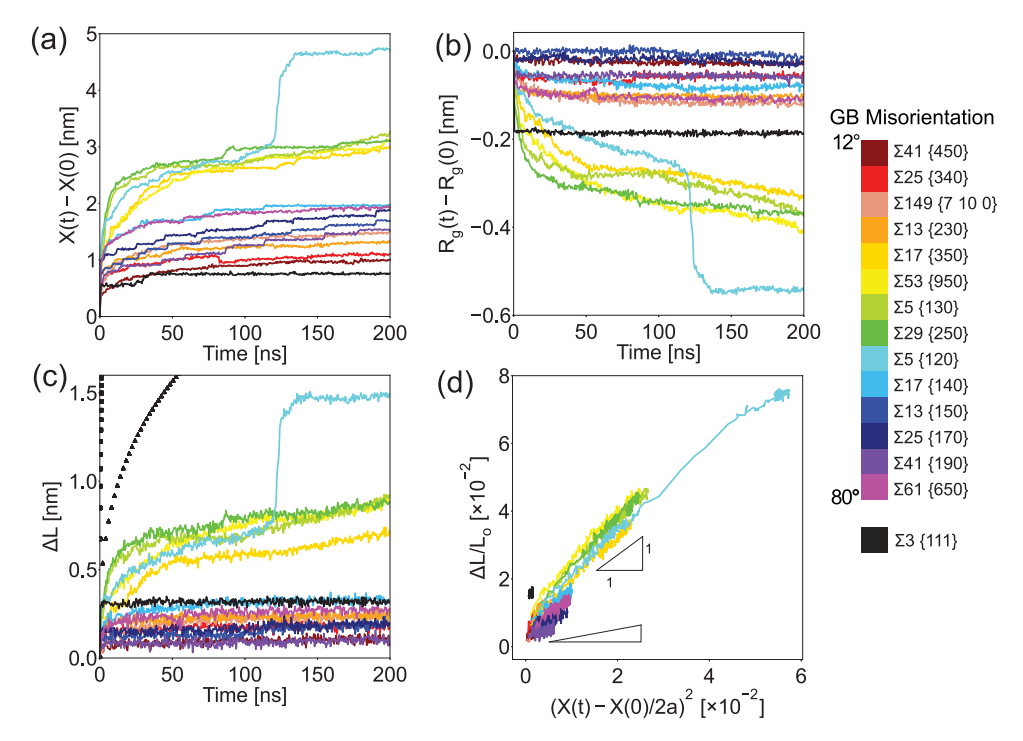


Figure 5. Temporal evolution of the (a) particle neck width X(t), (b) gyration radius $R_{\rm g}(t)$, and (c) change in distance between particles' centers $\Delta L = L_{\rm o} - L(t)$. (d) Plot of linear shrinkage $\Delta L/L_{\rm o}$ as a function of $[(X(t) - X(0))/2a]^{\mathcal{I}}$. In (d), time is implicit, which increases from lower left to upper right.

 \sum 29 {250}, \sum 53 {950}, and \sum 5 {130} GBs exhibit the largest decrease in R_g over time indicating faster densification rates.

The temporal evolution of $\Delta L = L_0 - L(t)$ is shown in Figure 5c, where it can be seen that some GBs are characterized by fast shrinkage kinetics and others reach a plateau in ΔL at very early simulation times. Again, the large jump in ΔL for the $\sum 5$ {120} GB system at t = 120 ns is correlated with the crystallographic orientation of particles and the resultant rapid change in GB misorientation. It can be seen that several GB systems are characterized by ΔL values that are slightly less than 0.5 nm, which for [001] tilt GBs is indicative of a shrinkage by an approximately one lattice plane. To correlate our simulation results with existing dynamical scaling sintering models, we follow the treatment by Johnson,²⁵ where $(\Delta L/L_{\rm o})^3 = (2.14 \gamma_{\rm s} \Omega \delta D_{\rm gb}/k_{\rm B} T a^4) t$ for a GB diffusion model, and use Ni surface energy $\gamma_{\rm s} \simeq 2.0~{\rm J/m}^2$, ⁶⁵ atomic volume $\Omega =$ 10.94 Å³, ⁶⁶ particle radius a = 10 nm, GB width $\delta = 1.0$ nm, and employ, as bounds, the smallest and largest GB selfdiffusion values from our calculations in Figure 2b. k_BT is the thermal energy, where $k_{\rm B}$ is Boltzmann constant. The analytical results are shown in Figure 5c (refer to Figure S5 in the Supporting Information for the same plot on a log-log scale), where the black square (triangle) markers denote the analytical model using the largest (smallest) GB self-diffusion values. It is evident that the analytical model overestimates shrinkage rates, even when using the smallest GB diffusion values. This suggests that sintering in nanoscale systems is not dominated by a single mechanism as suggested by the analytical models and also involves interface-related nucleation events, refer to Figure 4f–g for an example of the system with a $\sum 3$ {111} GB.

To correlate densification and particle neck growth during sintering, we plot linear shrinkage $\Delta L/L_o$ as a function of the square of normalized particle neck width $[(X(t) - X(0))/2a]^2$, and the results are shown in Figure 5d. Here, we note that time is implicit in this plot, which increases from lower left to upper

right.³⁰ Figure 5d permits a comparison of sintering rates with various GB types in terms of the temporal evolution of relevant geometric features. It can be observed that linear shrinkage in two-particle systems is a linear function of the square of the normalized particle neck width. By combining eq 2a and 2b, linear shrinkage is expressed as $\Delta L/L_o = (X/2a)^2$ assuming a single dominant mass transport mechanism, i.e., shrinkage is a linear function of the square of normalized particle width with a unit slope. Considerable variations, however, exist in the linear shrinkage—normalized particle neck growth behavior, in which several GB systems exhibit a smaller slope than the unit slope given by the shrinkage—square particle neck width relation. This suggests that several mechanisms are operative during nanoscale sintering as opposed to the single dominant transport mechanism assumption used to derive eq 2a and 2b.

The linear shrinkage and normalized particle neck width at the final sintering time t = 200 ns are obtained from Figure 5d and plotted in Figure 6 for all GBs explored in this work. The linear shrinkage $\Delta L/L_0$ is plotted on the ordinate and the markers are colored according to the normalized particle neck width values. For the sintering simulations attained in this work, the system with the $\sum 5$ {120} GB shows the largest densification followed by the ones with $\sum 29$ {250}, $\sum 53$ $\{950\}$, and $\sum 5 \{130\}$ GBs. While the 0 K energy of these GBs (cf. Figure 2a) is higher than the low-angle GBs explored in this work, these boundaries have the largest GB self-diffusion coefficients (cf. Figure 2b). Owing to the symmetry of the [001] axis in cubic crystals, a [001] tilt GB with a misorientation angle θ greater than $\pi/4$ is equivalent to one with $\pi/2 - \theta$. Therefore, the results depicted in Figure 6 suggest a trend, where sintering rates increase with the misorientation angle, at least for the [001] GBs explored in this

Finally, we examine the temporal evolution of particle neck curvatures as a function of GB geometry. According to eq 1a

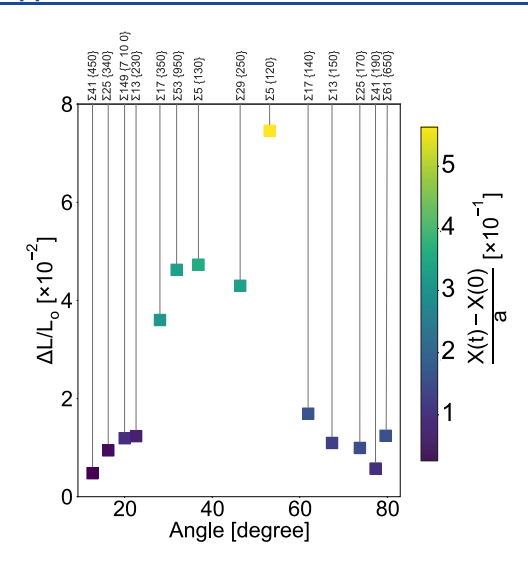


Figure 6. At the final sintering time t=200 ns, a plot depicting linear shrinkage $\Delta L/L_{\rm o}$ as a function of GB misorientation angle. Each data point is colored by its normalized particle neck width (X(t)-X(0))/a.

and 1b, the sintering stress and, thus, the chemical potential depends on the local curvature κ , and gradients in the chemical potential between particle neck regions and far-field free surface areas constitute a driving force for sintering. 1,27 Since our atomistic two-particle systems are periodic along the outof-plane direction (i.e., these are circular disks with a zero curvature along the out-of-plane direction), the relevant curvature is the one describing the particle neck radius, i.e., $\kappa \propto 1/r$. Figure 7 shows snapshots of representative atomistic two-particle systems at simulation times of (a1-d1) t=1 ns (top row), (b2-d2) t = 100 ns (middle row), and (a3-d3) t = 100200 ns (bottom row). Systems with $\sum 3$ {111} (Figure 7a1-a3), $\sum 41$ {450} (Figure 7b1-b3), $\sum 25$ {170} (Figure 7c1c3), and $\sum 5$ {120} (Figure 7d1-d3) GBs are shown. In all panels, curvatures at points on particle neck regions are represented by arrows, whose lengths are proportional to the magnitude of the curvature. In the early stages of sintering, κ in

particle neck regions of all systems are comparable in magnitude. For the system with a $\sum 3$ {111} GB, no considerable evolution of κ values is observed outside of an initial transient, which indicates sluggish sintering processes for this GB system. For the other GB systems depicted in Figure 7, κ values decrease with increasing sintering time. Further, the curvature exhibits asymmetric profiles between the left and right sides of the particle neck regions, which is indicative of varying dynamics and mass transport fluxes between both sides of particle neck regions. For example, Figure 7c3 shows large κ values on the left particle neck region compared to that on the right side.

The results depicted in Figure 7 are quantified by calculating the average curvature $\langle \kappa \rangle$ across both left and right sides of particle neck regions, and the results are shown in Figure 8 for a few representative systems, refer to Figure S6 in the Supporting Information for a plot of the average curvature for all systems explored in this work. Variations in $\langle \kappa \rangle$ profiles can be seen as a function of the GB type. In the initial stages, $\langle \kappa \rangle$ starts at large values, then decreases as the systems sinter. For the systems with $\sum 29$ {250} and $\sum 5$ {120} GBs, a rapid decrease in $\langle \kappa \rangle$ can be seen in the first ≈ 5 ns, while in those with $\sum 41 \{450\}$ and $\sum 25 \{170\}$ GBs, the decrease in $\langle \kappa \rangle$ is more gradual, i.e., over ≈ 100 ns. On the other hand, the $\langle \kappa \rangle$ profile remains flat for the system with a $\sum 3$ {111} GB, with some fluctuations due to the atomistic nature of two-particle systems. This is an indication that while the sintering driving force is large in the system with a $\sum 3$ {111} GB, its sintering kinetics are sluggish, at least for the simulation times attained in this work. Our curvature results provide a bridge that couples atomistic simulations to mesoscale sintering models, which employ sintering stress and, thus, curvature information, in its formulation.⁶⁷ Indeed, recent mesoscale computational studies have explored the evolution of sintering stress (i.e., curvature distributions) of whole particle compacts. 32,68

Our simulation results show that large variations exist in the temporal evolution of several geometric features, such as particle neck width X and curvature κ , and linear shrinkage $\Delta L/L_{\rm o}$ as a function of GB character, which in this work is defined by the tilt angle. While several studies have shown

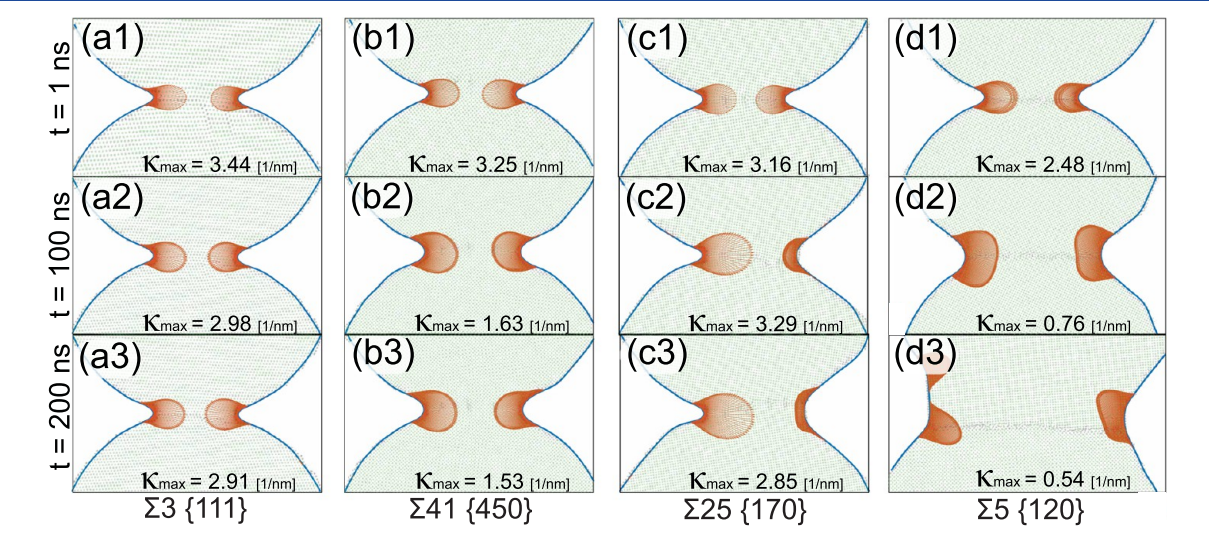


Figure 7. For two-particle systems with $(a1-a3) \sum 3 \{111\}$, $(b1-b3) \sum 41 \{450\}$, $(c1-c3) \sum 25 \{170\}$, and $(d1-d3) \sum 5 \{120\}$ GBs, temporal evolution of the local curvature at the particle neck regions at t=1 ns (top panels), t=100 ns (middle panels), and t=200 ns (bottom panels). Curvatures at particle neck regions are represented by arrows, whose lengths are scaled by the curvature values.

anisotropic sintering due to particle packing characteristics (i.e., particle size, shape, distribution, and spatial arrangements), ⁶⁹ internal pore geometry, ⁷⁰ size and number of particle contacts, ⁷¹ geometric constraints, ⁷² and sintering process parameters (e.g., solids loading, temperature), ⁷³ our results show that at atomic scale variations in local sintering stress (i.e., curvatures) as a function of GB character could be responsible for anisotropic sintering effects. This in turn indicates that the GB network topology is an important factor in the sintering of particle compacts, as it may control spatial variations in densification rates within the sintered object. Our results suggest that the deliberate control of particle rotations provides an avenue to control sintering rates. Indeed, several emerging manufacturing techniques employ externally applied fields to control particle rotation during sintering. ^{74,75}

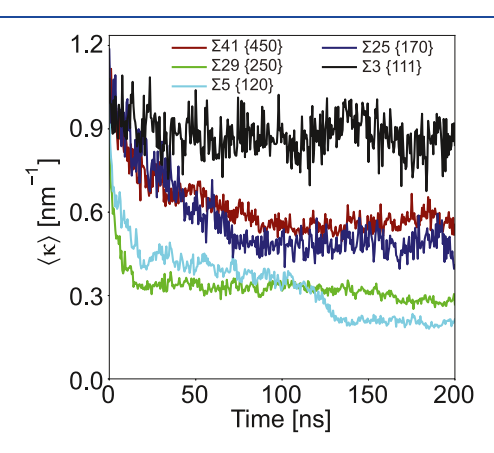


Figure 8. For two-particle systems with $\sum 3$ {111}, $\sum 5$ {120}, $\sum 25$ {170}, $\sum 29$ {250}, and $\sum 41$ {450} GBs, temporal evolution of the average curvature $\langle \kappa \rangle$ of the particle neck regions, which is a measure of sintering stress evolution.

■ CONCLUSIONS

In this study, we leveraged atomistic simulations to investigate the role of GB character in the sintering behavior of nanoscale Ni particles. To this end, a series of atomistic bicrystal systems with [001] tilt GBs and one with a $\sum 3$ {111} coherent twin GB were constructed. The atomistic bicrystals were then used to calculate the 0 K GB energy and obtain GB self-diffusion coefficients at 1000 K for all [001] GBs. Sintering simulations at 1000 K for 200 ns were conducted using the two-particle geometry, in which two 20 nm diameter particles from the atomistic blocks containing the GBs were carved out. Several geometric features, such as particle neck width, linear shrinkage, gyration radius, and particle neck curvatures, describing the morphological evolution during sintering were tracked over time. Simulation results revealed particle rotations, which were found to increase with the initial GB misorientation, that resulted in the temporal evolution of GB misorientation. The system with a $\sum 3$ {111} GB exhibited sluggish sintering kinetics, in which the particle neck grew in the early sintering stage through nucleation of GB defects. Our results showed large variations in particle neck growth and shrinkage rates as a function of GB type, where large misorientation angles resulted in increased sintering rates. Further, it was found that nanoparticles sinter at a much slower rate than predicted from diffusive sintering models, suggesting that nanoscale sintering is not dominated by a single

mechanism. As a measure of sintering stress, we tracked the temporal evolution of particle neck curvatures, which were shown to decrease over time at a rate dependent on GB geometry. On the whole, our modeling approach and simulation results provide future avenues to employ particle orientations and resultant GB types as a design tool in sintering-based manufacturing technologies to fabricate advanced materials with controlled microstructures.

ASSOCIATED CONTENT

Solution Supporting Information

The Supporting Information is available free of charge at https://pubs.acs.org/doi/10.1021/acsanm.1c01322.

Dimensions of the simulation box and number of atoms for each bicrystal system considered in this work; comparison of computational runtimes of cylindrical and 3D spherical particle geometries; a schematic illustrating the circular disk geometry used in this work compared to the spherical particle configuration; plot of system pressure as a function of time during the annealing step prior to the GB diffusion calculation; temporal evolution of particle neck width for representative cylindrical and 3D spherical particle geometries; temporal evolution of particle neck width for a representative GB system at several annealing temperatures; plot on a log-log scale of the distance between particles' centers as a function of time; and temporal evolution of the average curvature of particle neck regions for all systems explored in this work (PDF)

Web-Enhanced Feature

An animation in MPG format depicting the evolution of the two-particle system with a $\Sigma 5$ {120} GB along with particle rotation and particle neck curvature is available.

AUTHOR INFORMATION

Corresponding Author

Fadi Abdeljawad — Department of Mechanical Engineering, Clemson University, Clemson, South Carolina 29634, United States; Department of Materials Science & Engineering, Clemson University, Clemson, South Carolina 29634, United States; orcid.org/0000-0002-4495-4274; Email: fabdelj@clemson.edu

Authors

Omar Hussein — Department of Mechanical Engineering, Clemson University, Clemson, South Carolina 29634, United States; oocid.org/0000-0002-7856-9817

Maher Alghalayini — Department of Mechanical Engineering, Clemson University, Clemson, South Carolina 29634, United States; Oorcid.org/0000-0002-4071-0272

Shen J. Dillon – Department of Materials Science & Engineering, University of Illinois Urbana-Champaign, Urbana, Illinois 61801, United States; orcid.org/0000-0002-6192-4026

Complete contact information is available at: https://pubs.acs.org/10.1021/acsanm.1c01322

Notes

The authors declare no competing financial interest.

ACKNOWLEDGMENTS

F.A. acknowledges Clemson University Department of Mechanical Engineering through start-up funds. Clemson University is acknowledged for generous allotment of compute time on the Palmetto cluster. S.J.D. acknowledges support from the National Science Foundation under Grant no. DMR 1922867.

REFERENCES

- (1) Rahaman, M. N. Ceramic Processing and Sintering, 2nd ed.; Marcel Dekker, 2003.
- (2) Herring, C. *The Physics of Powder Metallurgy*; Kingston, W. E., Ed.; McGraw-Hill: NY, 1951; pp 143–179.
- (3) Buffat, P.; Borel, J.-P. Size effect on the melting temperature of gold particles. *Phys. Rev. A* **1976**, *13*, 2287–2298.
- (4) Greer, J. R.; Street, R. A. Thermal cure effects on electrical performance of nanoparticle silver inks. *Acta Mater.* **2007**, *55*, 6345–6349.
- (5) Lewis, J. Direct Ink Writing of 3D Functional Materials. Adv. Funct. Mater. 2006, 16, 2193–2204.
- (6) Saleh, M. S.; Hu, C.; Panat, R. Three-dimensional microarchitected materials and devices using nanoparticle assembly by pointwise spatial printing. *Sci. Adv.* **2017**, *3*, No. e1601986.
- (7) Ivanova, O.; Williams, C.; Campbell, T. Additive manufacturing (AM) and nanotechnology: promises and challenges. *Rapid Prototyp. J.* **2013**, *19*, 192–204.
- (8) Ko, S. H.; Pan, H.; Grigoropoulos, C. P.; Luscombe, C. K.; Fréchet, J. M. J.; Poulikakos, D. All-inkjet-printed flexible electronics fabrication on a polymer substrate by low-temperature high-resolution selective laser sintering of metal nanoparticles. *Nanotechnology* **2007**, *18*. No. 345202.
- (9) Skylar-Scott, M. A.; Gunasekaran, S.; Lewis, J. A. Laser-assisted direct ink writing of planar and 3D metal architectures. *Proc. Natl. Acad. Sci. U.S.A.* **2016**, *113*, 6137–6142.
- (10) Zhang, C.; Palko, J. W.; Rong, G.; Pringle, K. S.; Barako, M. T.; Dusseault, T. J.; Asheghi, M.; Santiago, J. G.; Goodson, K. E. Tailoring Permeability of Microporous Copper Structures through Template Sintering. ACS Appl. Mater. Interfaces 2018, 10, 30487—30494.
- (11) Bordia, R. K.; Kang, S.-J. L.; Olevsky, E. A. Current understanding and future research directions at the onset of the next century of sintering science and technology. *J. Am. Ceram. Soc.* **2017**, *100*, 2314–2352.
- (12) Nichols, F.; Mullins, W. Morphological changes of a surface of revolution due to capillarity-induced surface diffusion. *J. Appl. Phys.* **1965**, *36*, 1826–1835.
- (13) Burke, J. Role of Grain Boundaries in Sintering. *J. Am. Ceram. Soc.* **1957**, *40*, 80–85.
- (14) Bross, P.; Exner, H. Computer simulation of sintering processes. *Acta Metall.* **1979**, *27*, 1013–1020.
- (15) Uberuaga, B. P.; Vernon, L. J.; Martinez, E.; Voter, A. F. The relationship between grain boundary structure, defect mobility and grain boundary sink efficiency. *Sci. Rep.* **2015**, *5*, No. 9055.
- (16) Wakai, F.; Fukutome, H.; Kobayashi, N.; Misaki, T.; Shinoda, Y.; Akatsu, T.; Sone, M.; Higo, Y. Direct observation of sintering mechanics of a single grain boundary. *Acta Mater.* **2012**, *60*, 507–516.
- (17) McDonald, S.; Holzner, C.; Lauridsen, E.; Reischig, P.; Merkle, A.; Withers, P. Microstructural evolution during sintering of copper particles studied by laboratory diffraction contrast tomography (LabDCT). Sci. Rep. 2017, 7, No. 5251.
- (18) Vikrant, K.; Grosso, R. L.; Feng, L.; Muccillo, E. N.; Muche, D. N.; Jawaharram, G. S.; Barr, C. M.; Monterrosa, A. M.; Castro, R. H.; García, R. E. Ultrahigh temperature in situ transmission electron microscopy based bicrystal coble creep in zirconia I: Nanowire growth and interfacial diffusivity. *Acta Mater.* **2020**, *199*, 530–541.
- (19) Grosso, R. L.; Vikrant, K.; Feng, L.; Muccillo, E. N.; Muche, D. N.; Jawaharram, G. S.; Barr, C. M.; Monterrosa, A. M.; Castro, R. H.; García, R. E. Ultrahigh temperature in situ transmission electron

- microscopy based bicrystal coble creep in Zirconia II: Interfacial thermodynamics and transport mechanisms. *Acta Mater.* **2020**, 200, 1008–1021.
- (20) Kuczynski, G. C. Sintering Key Papers; Springer, 1990; pp 509–527.
- (21) Coble, R. Initial sintering of alumina and hematite. J. Am. Ceram. Soc. 1958, 41, 55–62.
- (22) Johnson, D. L.; Cutler, I. B. Diffusion sintering: I, initial stage sintering models and their application to shrinkage of powder compacts. *J. Am. Ceram. Soc.* **1963**, *46*, 541–545.
- (23) Tikare, V.; Braginsky, M.; Olevsky, E. A. Numerical simulation of solid-state sintering: I, sintering of three particles. *J. Am. Ceram. Soc.* **2003**, *86*, 49–53.
- (24) Martin, C.; Bordia, R. The effect of a substrate on the sintering of constrained films. *Acta Mater.* **2009**, *57*, 549–558.
- (25) Johnson, D. L. New method of obtaining volume, grain-boundary, and surface diffusion coefficients from sintering data. *J. Appl. Phys.* **1969**, *40*, 192–200.
- (26) Pan, H.; Ko, S. H.; Grigoropoulos, C. P. The solid-state neck growth mechanisms in low energy laser sintering of gold nanoparticles: a molecular dynamics simulation study. *J. Heat Transfer* **2008**, *130*, No. 092404.
- (27) Pan, J. Solid-state diffusion under a large driving force and the sintering of nanosized particles. *Philos. Mag. Lett.* **2004**, 84, 303–310.
- (28) Svoboda, J.; Riedel, H. Quasi-equilibrium sintering for coupled grain-boundary and surface diffusion. *Acta Metall. Mater.* **1995**, *43*, 499–506.
- (29) Pan, J.; Cocks, A. A numerical technique for the analysis of coupled surface and grain-boundary diffusion. *Acta Metall. Mater.* **1995**, 43, 1395–1406.
- (30) Djohari, H.; Derby, J. J. Transport mechanisms and densification during sintering: II. Grain boundaries. *Chem. Eng. Sci.* **2009**, *64*, 3810–3816.
- (31) Wang, Y. U. Computer modeling and simulation of solid-state sintering: A phase field approach. *Acta Mater.* **2006**, *54*, 953–961.
- (32) Abdeljawad, F.; Bolintineanu, D. S.; Cook, A.; Brown-Shaklee, H.; DiAntonio, C.; Kammler, D.; Roach, A. Sintering processes in direct ink write additive manufacturing: A mesoscopic modeling approach. *Acta Mater.* **2019**, *169*, 60–75.
- (33) Greenquist, I.; Tonks, M. R.; Aagesen, L. K.; Zhang, Y. Development of a microstructural grand potential-based sintering model. *Comput. Mater. Sci.* **2020**, *172*, No. 109288.
- (34) Seong, Y.; Kim, Y.; German, R.; Kim, S.; Kim, S.-G.; Kim, S. J.; Kim, H. J.; Park, S. J. Dominant mechanisms of the sintering of copper nano-powders depending on the crystal misalignment. *Comput. Mater. Sci.* **2016**, *123*, 164–175.
- (35) Zeng, P.; Zajac, S.; Clapp, P.; Rifkin, J. Nanoparticle sintering simulations. *Mater. Sci. Eng., A* **1998**, 252, 301–306.
- (36) Raut, J.; Bhagat, R.; Fichthorn, K. Sintering of aluminum nanoparticles: a molecular dynamics study. *Nanostruct. Mater.* **1998**, 10, 837–851.
- (37) Henz, B. J.; Hawa, T.; Zachariah, M. Molecular dynamics simulation of the kinetic sintering of Ni and Al nanoparticles. *Mol. Simul.* **2009**, 35, 804–811.
- (38) Sestito, J. M.; Abdeljawad, F.; Harris, T. A.; Wang, Y.; Roach, A. An atomistic simulation study of nanoscale sintering: The role of grain boundary misorientation. *Comput. Mater. Sci.* **2019**, *165*, 180–189.
- (39) Zhang, Y.; Wu, L.; El-Mounayri, H.; Brand, K.; Zhang, J. Molecular dynamics study of the strength of laser sintered iron nanoparticles. *Procedia Manuf.* **2015**, *1*, 296–307.
- (40) Moitra, A.; Kim, S.; Kim, S. G.; Park, S. J.; German, R. M.; Horstemeyer, M. F. Investigation on sintering mechanism of nanoscale tungsten powder based on atomistic simulation. *Acta Mater.* **2010**, *58*, 3939–3951.
- (41) Ch'ng, H.; Pan, J. Sintering of particles of different sizes. *Acta Mater.* **2007**, *55*, 813–824.

- (42) Song, P.; Wen, D. Molecular dynamics simulation of the sintering of metallic nanoparticles. *J. Nanopart. Res.* **2010**, *12*, 823–829.
- (43) Mao, Q.; Ren, Y.; Luo, K. H.; Li, S. Sintering-induced phase transformation of nanoparticles: A molecular dynamics study. *J. Phys. Chem. C* **2015**, *119*, 28631–28639.
- (44) Randle, V. Measurement of Grain Boundary Geometry; Taylor & Francis, 1993.
- (45) Olmsted, D.; Foiles, S. M.; Holm, E. Survey of computed grain boundary properties in face-centered cubic metals: I. Grain boundary energy. *Acta Mater.* **2009**, *57*, 3694–3703.
- (46) Foiles, S.; Hoyt, J. Computation of grain boundary stiffness and mobility from boundary fluctuations. *Acta Mater.* **2006**, *54*, 3351–3357.
- (47) Rohrer, G. S.; Holm, E. A.; Rollett, A. D.; Foiles, S. M.; Li, J.; Olmsted, D. L. Comparing calculated and measured grain boundary energies in nickel. *Acta Mater.* **2010**, *58*, 5063–5069.
- (48) Plimpton, S. Fast Parallel Algorithms for Short-Range Molecular Dynamics. *J. Comput. Phys.* **1995**, *117*, 1–19.
- (49) Stukowski, A. Visualization and analysis of atomistic simulation data with OVITO—the Open Visualization Tool. *Modell. Simul. Mater. Sci. Eng.* **2009**, *18*, No. 015012.
- (50) Larsen, P. M.; Schmidt, S.; Schiøtz, J. Robust structural identification via polyhedral template matching. *Modell. Simul. Mater. Sci. Eng.* **2016**, 24, No. 055007.
- (51) Stukowski, A.; Bulatov, V. V.; Arsenlis, A. Automated identification and indexing of dislocations in crystal interfaces. *Modell. Simul. Mater. Sci. Eng.* **2012**, *20*, No. 085007.
- (52) Lee, H.; Shabani, M.; Pataky, G. J.; Abdeljawad, F. Tensile deformation behavior of twist grain boundaries in CoCrFeMnNi high entropy alloy bicrystals. *Sci. Rep.* **2021**, *11*, No. 428.
- (53) Mishin, Y.; Farkas, D. Atomistic simulation of [001] symmetrical tilt grain boundaries in NiAl. *Philos. Mag. A* **1998**, 78, 29–56
- (54) Suzuki, A.; Mishin, Y. Atomic mechanisms of grain boundary diffusion: Low versus high temperatures. *J. Mater. Sci.* **2005**, *40*, 3155–3161.
- (55) Schneider, T.; Stoll, E. Molecular-dynamics study of a three-dimensional one-component model for distortive phase transitions. *Phys. Rev. B* **1978**, *17*, No. 1302.
- (56) Berendsen, H. J.; Postma, J. V.; van Gunsteren, W. F.; DiNola, A.; Haak, J. R. Molecular dynamics with coupling to an external bath. *J. Chem. Phys.* **1984**, *81*, 3684–3690.
- (57) Nosé, S. A unified formulation of the constant temperature molecular dynamics methods. *J. Chem. Phys.* **1984**, *81*, 511–519.
- (58) Hoover, W. G. Canonical dynamics: Equilibrium phase-space distributions. *Phys. Rev. A* **1985**, *31*, 1695–1697.
- (59) Li, S.; Fang, X.; Leng, J.; Shen, H.; Fan, Y.; Xu, D. A new route for the synthesis of Mg2B2O5 nanorods by mechano-chemical and sintering process. *Mater. Lett.* **2010**, *64*, 151–153.
- (60) Mishin, Y.; Herzig, C. Grain boundary diffusion: recent progress and future research. *Mater. Sci. Eng., A* **1999**, *260*, 55–71.
- (61) Nishiyama, T.; Seko, A.; Tanaka, I. Application of machine learning potentials to predict grain boundary properties in fcc elemental metals. *Phys. Rev. Mater.* **2020**, *4*, No. 123607.
- (62) Divinski, S. V.; Reglitz, G.; Wilde, G. Grain boundary self-diffusion in polycrystalline nickel of different purity levels. *Acta Mater.* **2010**, *58*, 386–395.
- (63) Chan, S.-W.; Balluffi, R. Study of energy vs misorientation for grain boundaries in gold by crystallite rotation method-II. Tilt boundaries and mixed boundaries. *Acta Metall.* **1986**, *34*, 2191–2199.
- (64) Lange, A. P.; Samanta, A.; Majidi, H.; Mahajan, S.; Ging, J.; Olson, T. Y.; van Benthem, K.; Elhadj, S. Dislocation mediated alignment during metal nanoparticle coalescence. *Acta Mater.* **2016**, 120, 364–378.
- (65) Zhang, W.-B.; Chen, C.; Zhang, S.-Y. Equilibrium crystal shape of Ni from first principles. J. Phys. Chem. C 2013, 117, 21274–21280.
- (66) Kitabjian, P.; Nix, W. Atomic size effects in Ni-Al based solid solutions. *Acta Mater.* **1998**, 46, 701–710.

- (67) Olevsky, E. A. Theory of sintering: from discrete to continuum. *Mater. Sci. Eng., R* **1998**, 23, 41–100.
- (68) Cardona, C. G.; Tikare, V.; Patterson, B. R.; Olevsky, E. On sintering stress in complex powder compacts. *J. Am. Ceram. Soc.* **2012**, 95, 2372–2382.
- (69) Raj, P. M.; Cannon, W. R. Anisotropic shrinkage in tape-cast alumina: Role of processing parameters and particle shape. *J. Am. Ceram. Soc.* **1999**, 82, 2619–2625.
- (70) Ch'ng, H.; Pan, J. Modelling microstructural evolution of porous polycrystalline materials and a numerical study of anisotropic sintering. *J. Comput. Phys.* **2005**, *204*, 430–461.
- (71) Wonisch, A.; Guillon, O.; Kraft, T.; Moseler, M.; Riedel, H.; Rödel, J. Stress-induced anisotropy of sintering alumina: Discrete element modelling and experiments. *Acta Mater.* **2007**, *55*, 5187–5199
- (72) Wakai, F.; Bordia, R. K. Microstructural evolution and anisotropic shrinkage in constrained sintering and sinter forging. *J. Am. Ceram. Soc.* **2012**, *95*, 2389–2397.
- (73) Patwardhan, J.; Cannon, W. R. Factors Influencing Anisotropic Sintering Shrinkage in Tape-Cast Alumina: Effect of Processing Variables. J. Am. Ceram. Soc. 2006, 89, 3019–3026.
- (74) Tanaka, S.; Makiya, A.; Kato, Z.; Uchida, N.; Kimura, T.; Uematsu, K. Fabrication of c-axis oriented polycrystalline ZnO by using a rotating magnetic field and following sintering. *J. Mater. Res.* **2006**, *21*, 703–707.
- (75) Suzuki, T. S.; Uchikoshi, T.; Sakka, Y. Effect of sintering conditions on microstructure orientation in α -SiC prepared by slip casting in a strong magnetic field. *J. Eur. Ceram. Soc.* **2010**, 30, 2813–2817